Article

Tracking lithospheric delamination and surface processes across the Messinian salinity crisis

Frédéric Mouthereau [1,2] ✉, **Louise Boschetti** [1,3], **Marine Larrey**[1,4], **Stéphanie Brichau**[1], **Nicolas E. Beaudoin**[2], **Damien Huyghe**[5], **Nick M. W. Roberts** [6] **& Mathieu Daëron**[7]

Lithospheric delamination involves short-lived crustal and surface responses, alkaline magmatism, high heat flow and extension. In the Western Mediterranean, delamination is hypothesized to have triggered uplift at the origin of the Messinian Salinity Crisis (MSC). But delamination as the primary cause of uplift is questioned due to the insufficient temporal resolution. We report new U-Pb ages and clumped isotope analyses from calcite veins formed in an eastern Betic intramontane basin. They reveal a brief fluid event from 8.5 to 5 Ma linked to extension and retreating delamination. After extension, shortening and uplift began at 4.5–3 Ma across the boundary between the Cabo de Gata arc basement and the Iberia margin. We show that the MSC occurred before shortening and during delamination. Slab detachment caused the demise of the MSC, the formation of a new plate boundary fault and tectonic escape between Africa and Iberia around 5 Ma.

Delamination is a process by which the lithospheric mantle or/and lower crust are detached and lost in the asthenosphere[1,2]. It provides an efficient mechanism to recycle crust and mantle into the convective mantle[3,4], and it also explains the differentiation of the continental crust in an arc setting[5,6] and in early Earth without involving two-plate subduction processes[7,8]. In late-/post-collision settings, continental delamination reflects the sinking of a negatively buoyant thickened or intrinsically dense lithosphere[9–11] or accompanies slab rollback by decoupling the mantle lithosphere from the overlying orogen as illustrated in the Western Mediterranean, such as the Apennines[12,13] and the Betic-Rif arc[14–17]. Eventually, the delaminated slab detaches (lithospheric tearing or break-off) leading to the development of new plate boundary faults, tectonic escape, and uplift, e.g., Anatolian Plateau uplift and the formation of North and East Anatolian Faults[18–21]. As delamination involves the replacement of the lithosphere by the asthenosphere, it leads to complex and short-lived crustal and surface responses, including uplift, alkaline magmatism, high heat flow, and extension. The rapid succession in time of these processes is a major difficulty in distinguishing between the causes and effects of delamination.

In the Betic-Rif arc (Fig. 1), it has been suggested that delamination, witnessed in the eastern Betics through post-collisional mantle-derived magmas at 6.3 Ma, caused the uplift of the Alboran continental margin[15]. This triggered the Messinian Salinity Crisis (MSC, 5.97–5.33 Ma) by closing the marine gateways between the Atlantic and the Mediterranean in the Betic Corridor (Spain) and the Rifian Corridor (Morocco)[15,22]. Delamination is, however, not the unique mechanism invoked for pre-MSC uplift, as it is synchronous with the onset of shortening presented as the major driver of pre-MSC late Tortonian uplift of the Betics (<7.8−7.3 Ma) and in the Rifian Corridor (7.0−7.2 Ma)[23,24]. Alternatively, both mechanisms can be at play. For instance, numerical models have suggested that the westward propagation of slab tearing, and detachment following delamination, stalled by around 8 Ma, resulting in resisting forces in the mantle that can

[1]GET, Université de Toulouse, UPS, CNRS, IRD, Toulouse, France. [2]Université de Pau et des Pays de l'Adour, E2S UPPA, CNRS, TOTAL, LFCR, Pau, France. [3]Université Grenoble Alpes, ISTerre, Grenoble, France. [4]TotalEnergies SE, CSTJF, Pau, France. [5]Centre de Géosciences, MINES ParisTech, Fontainebleau, France. [6]Geochronology and Tracers Facility, British Geological Survey, Nottingham, UK. [7]Laboratoire des Sciences du Climat et de l'Environnement, LSCE/IPSL, Université Paris-Saclay, CEA-CNRS-UVSQ, Gif-sur-Yvette F-91191, France. ✉e-mail: frederic.mouthereau@get.omp.eu
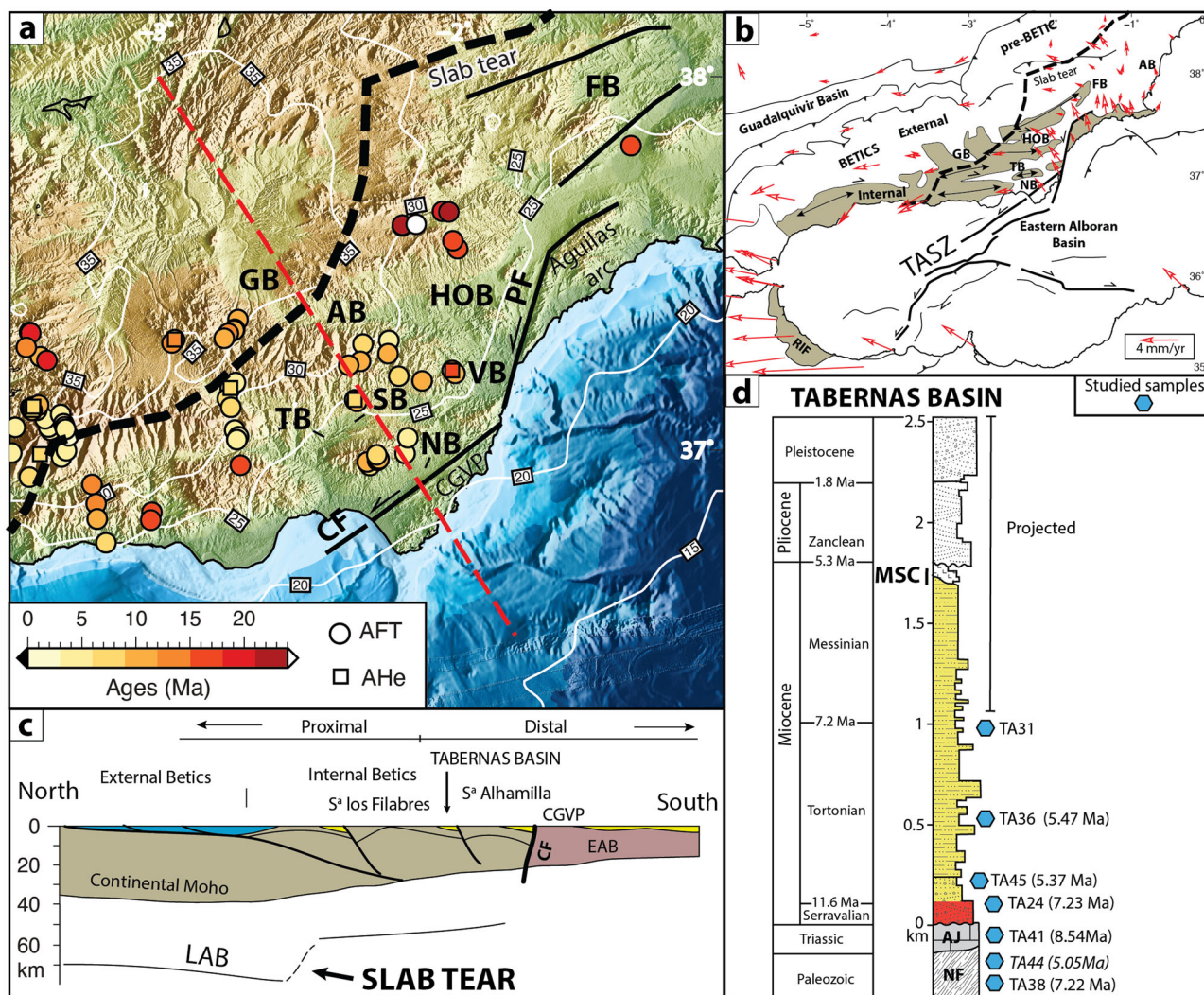
Fig. 1 | Main tectonic features, deep structure of the eastern Betics, and stratigraphy of the Tabernas basin. a Topography with existing low-temperature thermochronology dates inferred from Apatite fission-track (AFT) and (U-Th-Sm)/He (AHe) analyses are shown in addition to crustal thickness (labeled white thin lines), location of slab tear (thick back dashed lines) main faults and Neogene intramontane basins. **b** GNSS-based velocities (red vectors) in southern Spain with the location of External Zone and Internal Zone (brown filled polygons) of the Betic Cordillera after ref. 30. **c** Lithosphere-scale cross-section of the eastern Betics (see location as red dashed line in **a**). **d** Stratigraphy of the Tabernas Basin with rock samples from the Paleozoic basement of Nevado-Filábride complex (NF), the Triassic limestones of the Alpujárride complex (AJ) to the Serravallian-Tortonian siliciclastic deposits. TASZ Trans-Alboran Shear Zone.

explain uplift and the current tectonic activity[25], notably the formation of a new convergent plate boundary between Iberia and Africa[26]. Other numerical scenarios have linked the pre-MSC uplift to lithospheric rebound induced by lithospheric tearing modulated by the obliquity of the convergence relative to the Iberian paleomargin[27]. Additional processes like the emplacement of a thick buoyant arc in the Eastern Alboran Basin (EAB) contributed to the emergence of the Alboran domain before the MSC from 10 to 6.2 Ma, and a land bridge might have persisted between Africa and Iberia during and after the MSC from 7 to 3 Ma[28].

The exact relationships between uplift, onset of indentation, and mantle-derived process have not yet reached sufficient temporal resolution to allow a clear distinction between delamination, detachment, and shortening as the main drivers of the uplift and exhumation that led to the MSC. Here, we investigate the case of the eastern Betics where the continental basement of Alboran, now accreted to the southern Iberia paleomargin and intruded by mantle-derived magmas, is indented by the magmatic arc of the EAB, represented by the Cabo de Gata Volcanic Province (CGVP), and the rotated and sheared units of the Alboran basement in the Águilas Arc (Fig. 1a, b). Geodetic data

shows that indentation is accommodated by the extrusion of the Alboran block bounded to the north by a broad zone of East-West right-lateral transtensional shear in the Betics, and by the left-lateral movement of the Carboneras Fault (CF) and Palomares Fault (PF) to the south-east, which continues as transpressional left-lateral shear in the Rif[29,30]. These fault segments are part of the Trans-Alboran Shear Zone (TASZ), a 400-km-long left-lateral fault network crossing the whole Alboran basin (Fig. 1b). The current tectonic context is the result of a complex geodynamic evolution of the Betic-Rif arc that began with subduction in the Eocene. Details of plate kinematics are debated but a consensus exists on the fact that from around 20 Ma, the Betic orogenic belt collapsed leading to the opening of the Alboran basin controlled by the westward retreat of the Gibraltar slab and delamination[31]. The different motion between the retreating slab domain (Alboran) and the upper plate (Iberia) caused highly oblique crustal thinning in the continental basement of the Alboran Basin throughout the Langhian to Tortonian (16-8 Ma), which led to the exhumation of E-W metamorphic domes and subsidence in intermontane basins of the Internal Betics[32]. The Gibraltar slab is now imaged resting at 600 km below the Alboran Sea[22], and its northern edge, forming part of the

Iberia continental lithosphere, is detached over 400 km (Fig. 1b) below the Betics from the Lorca basin to the region of Malaga[33].

As a result of extension, the internal intramontane basins (Fortuna-Lorca, Guadix-Baza, Huercal-Overa, and Almanzora basins) and external basins (Tabernas, Sorbas, Vera, Alicante-Cartagena, Nijar-Carboneras basins) are distinguished according to their position on the margin, proximal and distal, respectively (Fig. 1a–c). Within the more distal margin, the external Tabernas basin represents an E-W-trending basin filled by Serravallian-Tortonian continental to late Tortonian deep marine deposits[34] resting at ~400 m above sea level between the metamorphic domes of Sierra de Alhamilla and Sierra de los Filábres (Fig. 1a–d).

Key unknowns include the duration of extension in the Tabernas basin and its relationship to transitions with uplift, mantle-derived magmatism, slab detachment, and initiation of contraction in the eastern Betics, specifically the onset of the Carboneras plate boundary fault. To resolve these issues, we analyze new U-Pb dates tied to clumped-isotope temperatures of syn-extension calcite-filled fractures from the Tabernas basin, with a view to constraining the transition in intramontane basins from extension to compression and uplift, along with lithosphere thermal conditions. Results are compared to key transitions resolved by the analysis of the cooling evolution of the CGVP and the continental basement using apatite (U-Th-Sm)/He (AHe) thermochronology. We examine the relationships between the lithosphere structure, the thermal state in the mantle and analyze the isostatic/dynamic support of the topography. The comparison with existing age constraints on exhumation and short-lived phases of magmatism enables us to more accurately identify the mechanisms that were active before and during the Messinian Salinity Crisis, likely contributing to the onset of Mediterranean isolation.

Results

Carbonate U-Pb dating of syn-extension fractures

Carbonate samples in syn-extension fractures (veins, faults) (Supplementary Data 1) were selected along a section comprising the metamorphic basement of the Tabernas basin, exposed on the flank of the Sierra de los Filábres, and Tortonian-Messinian sediments, in the center of the basin, for in-situ Laser Ablation Inductively Coupled Plasma Mass Spectrometer (LA-ICPMS) U-Pb geochronology. Basement samples comprise high-grade schists of the Nevado-Filábride (NF) complex (TA38, TA44) and Triassic marbles of the Alpujárride complex (TA41) that yield carbonate U-Pb ages of 7.22 ± 0.79 Ma (TA38, $n = 51$, 2σ), 5.05 ± 0.27 Ma (TA44, $n = 112$, 2σ) and 8.54 ± 0.21 Ma (TA41, $n = 25$, 2σ) (Figs. 1d and 2). Calcite from veins collected in lower Tortonian continental deposits (TA45, TA24) yield U/Pb ages of 5.37 ± 0.25 Ma (TA45, $n = 124$, 2σ) and 7.23 ± 0.60 Ma (TA24, $n = 84$, 2σ). Note that TA24 was sampled in lower Tortonian conglomerates exposed in the Tabernas topographic ridge, a structure interpreted as a strike-slip fault (Fig. 1d). The carbonate U-Pb date in the upper Tortonian marine turbidites (TA36) is 5.47 ± 0.23 Ma ($n = 75$, 2σ).

Clumped-isotope temperatures of fluids

Among these U-Pb dated samples, five (TA24, TA36, TA38, TA41, TA45) were jointly analyzed for clumped isotope temperatures (T_{47}) and oxygen isotopic values of the mineralizing fluids (Fig. 3) (see also Supplementary Data 2). Samples from the Nevado-Filábride (TA38) and Alpujárride complexes (TA41) show similar precipitation temperatures T_{47} of 66.9 ± 4.4 °C ($n = 3$) and 63.7 ± 4.2 °C ($n = 3$) (°C ± 95%), corresponding to equally close values of $\delta^{18}O_{water}$ of 0.7 ± 0.7‰ VSMOW and -0.9 ± 0.7‰ VSMOW, respectively. Lower Tortonian continental deposits (TA45, TA24) yield higher T_{47} of 76.2 ± 4.8 °C and 84.5 ± 5.0 °C, and the fluid composition also show contrasted $\delta^{18}O_{water}$ of -4.6 ± 0.7‰ VSMOW (TA45) and 3.1 ± 0.7‰ VSMOW (TA24). Upper Tortonian marine sediments (TA36) indicate a precipitation temperature of 76.7 ± 4.8 °C and isotopic composition of fluids $\delta^{18}O_{water}$ of

0.3 ± 0.7‰ VSMOW. The TA31 sample for which we have no U-Pb date was collected in the upper Tortonian channelized turbidites, south of the Tabernas topographic ridge, in a stratigraphic level only slightly younger than TA36. It yields a T_{47} of 56.4 ± 3.9 °C and $\delta^{18}O_{water}$ of -5.2 ± 0.7‰ VSMOW.

Apatite (U-Th)/He dating of volcanic and metamorphic rocks

Five AHe ages from apatites with aliquots that replicate well were obtained in CGVP rhyolite (MOJ1.3, $n = 4$), dacite (MOJ1.4, $n = 4$) and andesite (MOJ1.1, $n = 4$; MOJ1.2, $n = 5$; MOJ1.5, $n = 3$) (Supplementary Data 3). Results show single-grain alpha-ejection corrected AHe ages between 10.8 ± 0.9 Ma and 3.1 ± 0.2 Ma. Mean AHe ages range in andesites from 4 ± 0.2 Ma (2σ) for MOJ1.1, 9.1 ± 0.3 Ma for MOJ1.2 and 6.1 ± 0.3 Ma for MOJ1.5, and consistent AHe ages of 7.0 ± 0.3 Ma for dacite MOJ1.4 ($n = 4$) and 5.9 ± 0.2 Ma for rhyolite MOJ1.3 ($n = 4$). West of the Carboneras fault, only one sample out of five originally collected in the NF metamorphic basement yielded enough apatite grains suitable for AHe analyses. MOJ2.1 ($n = 3$) sampled at 520 m in NF micaschists east of the Sierra de los Filábres yielded the youngest mean AHe age of 2.6 ± 0.1 Ma. The scarcity of apatite in NF micaschists and their low Uranium content (0.5-1.4 ppm for MOJ2.1) has already early been noticed[35]. We note that in the region of the NF micaschists (Sierra Alhamilla) where these previous apatite-fission track analyses have been successful, apatite yielded slightly older ages of 5.7 ± 1.1 Ma and 6.1 ± 1.2 Ma. An AHe age of 15.2 ± 0.8 Ma was obtained close to MOJ2.1 (elevation 2000 m) but it is more problematic considering it is similar to its apatite-fission track age of 15.6 ± 1.9 Ma[36]. The eU-age and (U-Th)/age relationships of our AHe-dated apatite samples show a positive correlation that agrees with the expected increase of closure temperature as a function of radiation damage[37].

Time-temperature histories

Reconstruction of time-temperature histories of CGVP have been reconstructed based on simple thermal inputs assuming that published $^{40}Ar/^{39}Ar$ ages[16,38] faithfully represent the timing of magma cooling below 350 ± 50 °C (Tc 350 °C on biotite), and that the timing of cooling at surface temperature (20 ± 20 °C) is indicated by the deposition of Tortonian-Messinian marine limestones on top of sampled CGVP lavas (Fig. 4). These deposits attest to emersion as early as 10–9 Ma (lower Tortonian) while other stratigraphic contact suggests later emersion until the Messinian[39,40]. As the sampled dacite, andesite, and rhyolite from CGVP were emplaced at the surface, cooling is expected to be instantaneous on the geological timescales. However, the large majority of AHe ages (closure temperature of 70-50 °C) in CGVP are younger than the $^{40}Ar/^{39}Ar$ ages of their parental volcanic rocks (11 ± 1 Ma) by 7 to 2 myrs. The delay between magma crystallization of calc-alkaline suites and AHe cooling ages reveals a complex cooling history caused by subsequent punctual thermal events. This may represent the effect of pyroclastic eruptions or lava flow, doming or caldera collapse, circulation of hydrothermal fluids linked to Cu–Au mineralization well documented during the CGVP formation[41] and burial heating by Tortonian-Messinian to Pliocene deposits. Modeling results show that all volcanic rocks cooled below 350 ± 50 °C at different rates between 12 and 8 Ma, which marks the end of the volcanic phase. After 8 Ma, samples variably recorded the deposition of the upper Tortonian-lower Messinian carbonate platform. Samples from the southern half of CGVP MOJ1.2 to MOJ1.5 show no significant heating or cooling, or it is within the uncertainties of surface temperature, hence indicating no measurable exhumation (Fig. 4). By contrast, in the north, where lower Messinian and lower Pliocene marine deposits are preserved, MOJ1.1 thermal evolution shows burial heating below sediments followed by cooling at ca. 4.5 Ma. For thermal history modeling of the MOJ2.1 micaschist sample, we have used published AHe and AFT data from a sample collected nearby. Model shows that MOJ2.1 resided at 120-80 °C (Tc AFT) and possibly 70-50 °C (Tc AHe) at
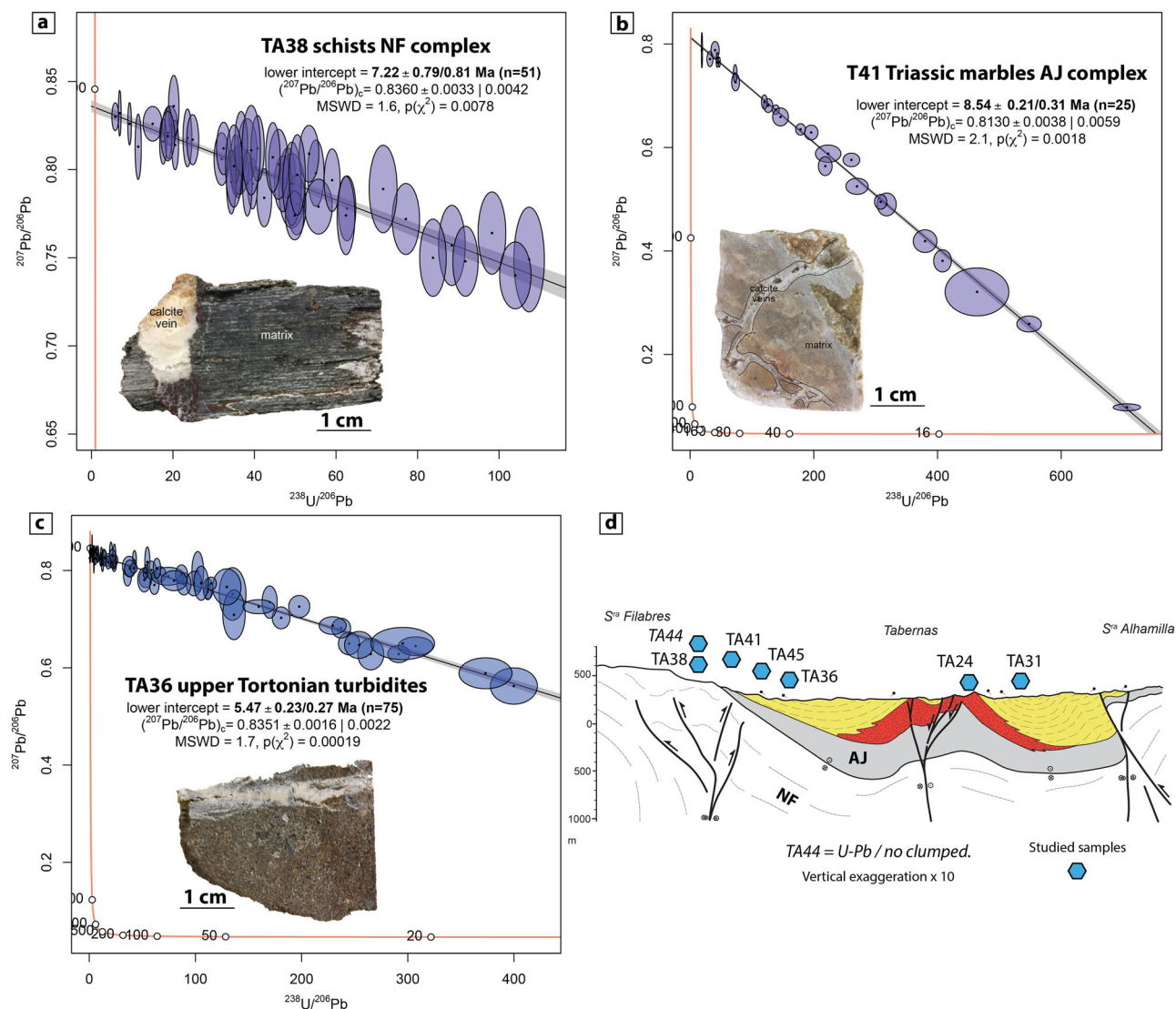
Fig. 2 | Tera-Wasserburg diagrams of a selection of samples. a Sample TA38 from the Nevado-Filábride complex, **b** sample TA41 from the Alpujárride complex and **c** sample TA36 from upper Tortonian deposits of the Tabernas basin (all results are presented in Supplementary Data 1). **d** Cross-section shows the spatial distribution of samples across the Tabernas basin (layers have the same color code as Fig. 1d).

15 ± 1 Ma, and cooled at ca. 3 Ma (Fig. 4). We infer that both CGVP volcanic rocks (MOJ1.1) and metamorphic basement (MOJ2.1) north of CF cooled between 4.5 and 3 Ma, clearly after the MSC, at a rate between 36 °C/Myr (MOJ1.1) and 48 °C/Myr (MOJ2.1).

Impact of mantle-derived processes on topography

The mean elevation of the Central-Eastern Betics (Fig. 5a) region is 868 m with the highest elevation of 3467 m in the Sierra Nevada. Receiver functions and reflection seismic data[42] reveal a bimodal distribution of crustal thicknesses ranging from 35 km in the north to 25 km in the south and east (Figs. 1a and 5a), expressing crustal and lithosphere thinning south of the Sierra Nevada, Sierra de los Filábres and Sierra de las Estancias, linked to the oblique opening of the Alboran basin[43]. Crustal thinning onshore is reflected in the topographic decrease down to 176 m south of Sierra de los Filábres and in Cabo de Gata (Fig. 5a). The crustal thickness offshore reduces to 15 km in the EAB (Fig. 1a). To compare current topography with predictions using isostatic calculations, the lithosphere thickness across the eastern Betics was inferred from various seismic tomography models SL2013sv[44], LITHO1.0[45], and Mean model[46] (Fig. 5a). From these models, upper and lower bounds for the lithosphere thickness fall between

65 km and 50 km. The value of 65 km fits both SL2013sv and Mean models. It is also consistent with maximum depths for the lithosphere of about 60 km (1.8 GPa) independently determined from thermobarometric calculations on Neogene mantle-derived K-rich basalts (MgO > 8 wt.%, SiO_2 > 45 wt.%)[47]. This value is within the range of thicknesses <100 km for fertile and hot phanerozoic sub-continental lithosphere[48], a feature characteristic of the European lithosphere[49].

Elevation is calculated for a column of continental lithosphere with respect to the depth of a standard mid-ocean ridge, assuming pressure-temperature dependent densities and chemical depletion for the lithospheric mantle[50] (Supplementary Discussion). Results show that for a lithosphere thickness of 65 km, the calculated elevation is negative (−250 m), assuming a crustal thickness of 25 km (Moho depth below Tabernas Basin), an average crustal density of 2.7 based on EPcrust model[51], and a reference density for the lithospheric mantle of 3.3 (Fig. 5b); it is null for lithosphere thickness of 50 km and −500 m for a 70 km-thick lithosphere (Fig. 5c). The lithosphere below the eastern Betics is therefore not in isostatic equilibrium unless we assume a mantle density decrease of 80-100 kg/m⁻³. Studies of rifted margins show that the formation of light mineral phases such as plagioclase during extension and shallowing of the lithospheric mantle can
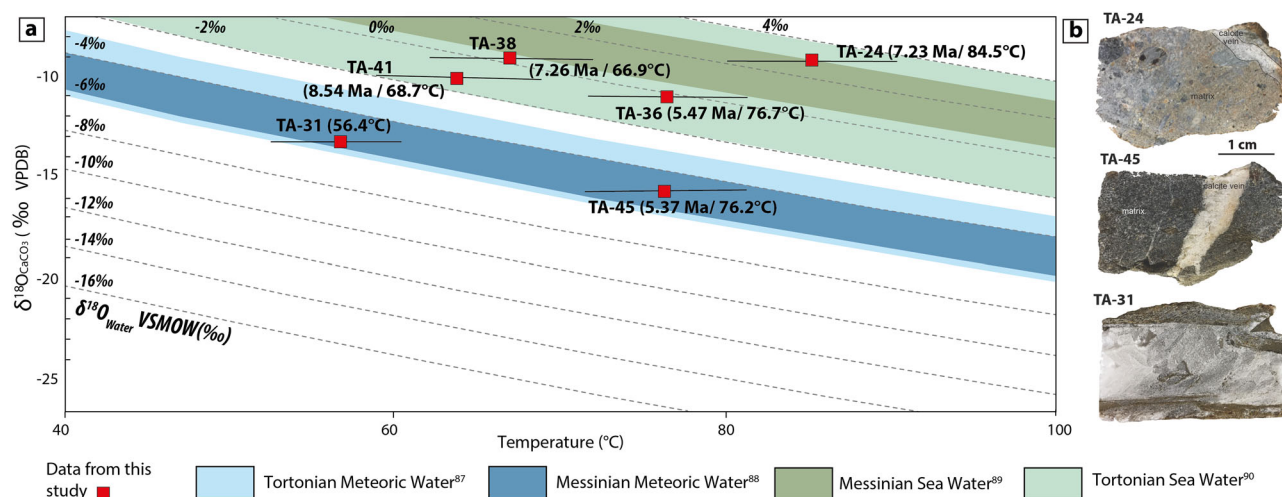
Fig. 3 | Measured oxygen isotopic composition δ¹⁸O$_{calcite}$ of the U-Pb-dated vein cement (‰ VPDB) against precipitation temperature (°C). a Precipitation temperatures obtained from clumped-isotope analyses are depicted along with uncertainties reported as ±2σ. Oblique lines are the calculated oxygen isotopic values of the mineralizing fluids δ¹⁸O$_{water}$ (see "Methods" section). **b** Photographs show a selection of analyzed hand samples. Numbers in parentheses are U-Pb ages and T$_{47}$. The composition of seawater and meteoric water composition in Tortonian and Messinian are from refs. 87–90.

produce a density decrease of mantle rocks down to 3.2 at 60 km for temperatures above 800 °C[52]. This is likely to have occurred in the Betics during the Mesozoic extension as the lithospheric mantle was refertilised by tholeiitic MORB-like melts[53]. Alternatively, elevation can also be well reproduced by the upwelling of hot asthenosphere, likely with a fraction of melt as indicated by low S-wave velocity domain of 4.2 km.s⁻¹ around 100 km (Fig. 5a). Based on the parametrization of shear wave velocity-temperature[54] we determine anomalously high sub-lithospheric temperatures of 1550 °C. Such a low viscous channel could easily explain the observed mean topography of 500 m around Tabernas Basin (see "Methods" section and Supplementary Discussion). We infer that the compositional variations in the mantle lithosphere and asthenospheric upwelling likely acted together and contributed to the support of the eastern Betic topography.

Discussion

Pre-MSC uplift and subsidence driven by mantle delamination

The timing of uplift in the eastern part of the Betics has been provided in recent research by the age of the marine-continental transition in the intermontane basins. In the internal basins of Fortuna-Lorca, Guadix-Baza Huercal-Overa, and Almanzora, the transition has been dated to the end of the Tortonian (8–7.5 Ma), indicating uplift before the MSC[23,55–58]. It has also been suggested that the onset of N-S/NW-SE shortening occurred around 8–7 Ma in the eastern Betics[34,59,60] and in the Alboran Sea[61]. This timing is in line with previous T-t paths inferred from apatite fission tracks (AFT) ages ranging from 2.5 Ma to 25 Ma (mode of 8 Ma; Fig. 1a)[35,36,62–65] that support the interpretation that exhumation in the Internal Zone was progressive and associated with orogen-parallel stretching from the Sierra de los Filábres at 13–11 Ma (Serravallian-Tortonian) to the Sierra de Nevada at 8–6 Ma (Late Tortonian-Messinian). The late Tortonian uplift and exhumation documented in the internal basins therefore appear temporally closely related to a late Tortonian stage of extension. At lower elevation, in external basins that recorded the MSC, the marine-continental transition shows a younger uplift ranging from Pliocene, ca. 5.3 Ma in Sorbas Basin, to post-mid-late Pliocene (4-3.6 Ma) for distal Vera, Alicante-Cartagena, Nijar-Carboneras basins[55,58,66]. The final uplift in the external basins occurred therefore after the Zanclean reconnection between the Atlantic and Mediterranean.

The U-Pb ages, isotopic signatures, and temperatures of carbonate fluids in veins from the Tabernas basin are representative of the

thermal conditions and fluid pathways that prevailed during extension in external basins. The narrow U-Pb age range from 8.5 to 5 Ma argues for a short-lived fluid event, for which the cessation coincides with a change in the tectonic stress field. This scenario is further argued by the differential exhumation across the CF between the CGVP (MOJ1.1) that cooled from 4.5 Ma and the NF metamorphic complex (MOJ2.1) that cooled from 3 Ma. We interpret this difference as evidence for sequential deformation from south to north associated with the movement across the CF as the CGVP and Águilas Arc collided with the continental basement. The initiation of cooling across the CF is coincident with the termination of fluid circulation and uplift of the external basins. We infer that the end of fluid circulation marks the onset of shortening across the CF at 4.5 Ma that regionally coincides with the onset of collision between the continental basement and the magmatic arc crust of EAB. The Pliocene compression is synchronous with the post-MSC uplift in external basins and is distinct from the late Tortonian, pre-MSC uplift, documented in internal basins, which is associated with extension in the Betics and transpression in the Rif.

The different timing of uplift between internal (8-7.5 Ma) and external basins (post-5 Ma) is significant and has acted at different scales. For instance, the late Tortonian uplift is described as nearly synchronous across the whole of the Betics, even farther westward of the tip of the slab tear[23,57], and in the Rif. If this late Tortonian uplift in the internal basin is compared to the age and type of magmatism in eastern Betics, it appears to coincide with a transition from post-collisional calc-alkaline volcanism (basaltic andesite, andesite, dacite, rhyolite), older than 8 Ma in CGVP (mostly 11 ± 1 Ma) and Alboran Sea, to high-K calc-alkaline, shoshonitic and ultrapotassic volcanism (Si-K-rich lamproite) dated between 8 and 6 Ma, mean ages of 7.4 Ma[16,67,68] (Fig. 6). These mantle-derived lavas are found preferentially north of CGVP and south of the slab edge (Fig. 6) where asthenosphere upwelling is imaged by low S-wave velocity anomaly (Fig. 5).

Control of mantle-driven processes on late Tortonian syn-extension fluids can be tested in the Tabernas basin based on clumped-isotope water composition and temperatures. Comparison of δ¹⁸O$_{water}$ inferred from samples δ¹⁸O$_{calcite}$ (Fig. 3) with the oxygen isotope composition of Tortonian and Messinian seawater and freshwater supports an interpretation that the fluids originated from two distinct sources. Values of δ¹⁸O$_{water}$ between −0.9 ± 0.7‰ VSMOW and +3.1 ± 0.7‰ VSMOW (T24, T36, T38, T41) reveal they precipitated in equilibrium with marine water or involved a component of formational
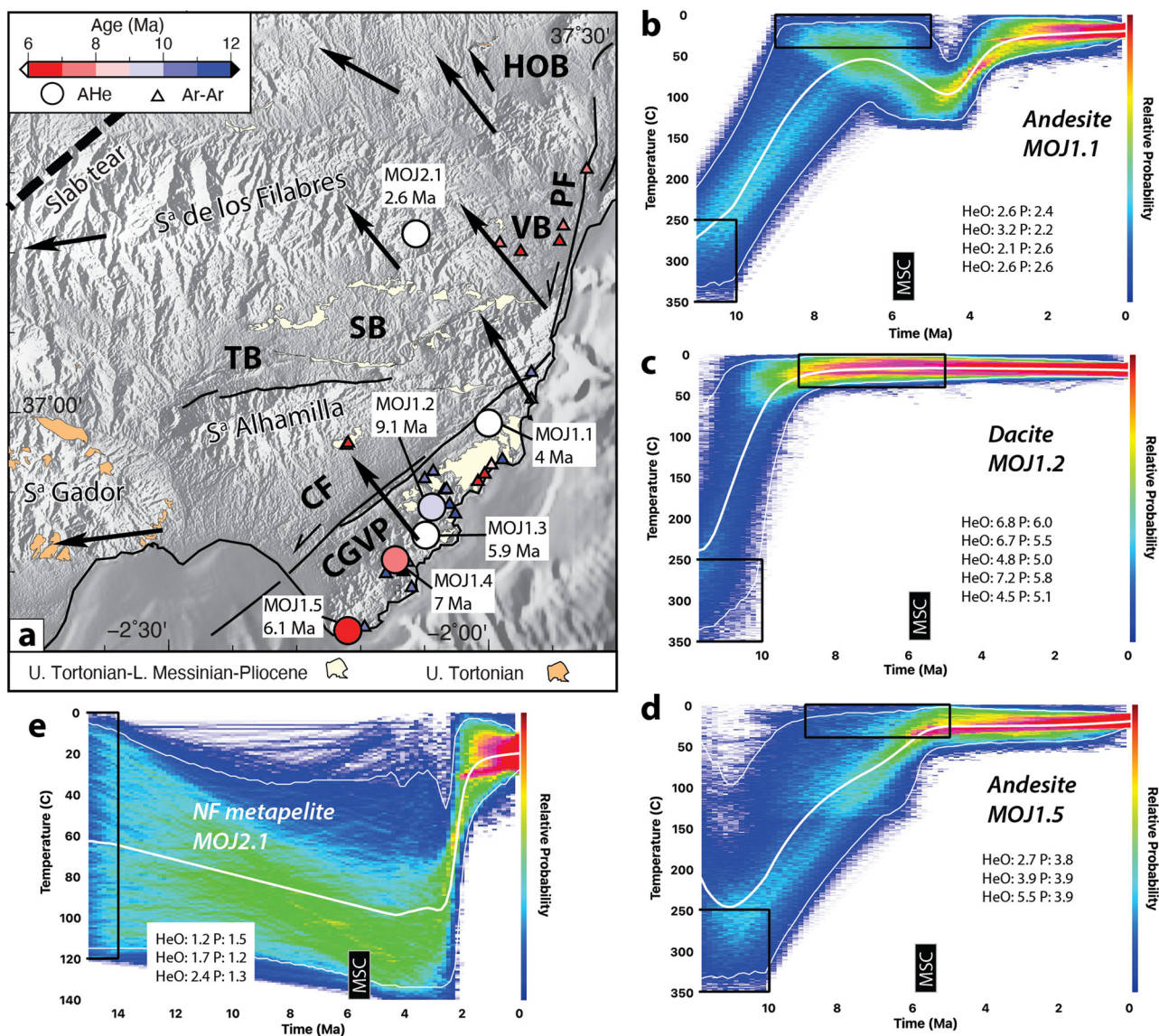
Fig. 4 | (U-Th)/He ages and time-temperature histories. a AHe ages (circles) obtained in the Cabo de Gata Volcanic Province and the Sierra de los Filábres (metamorphic Nevado-Filábride complex) (see Supplementary Data 3). Black vectors are GNSS-based velocities. Note that NW-directed velocities diminish towards the north (e.g., between CGVP and Sierra de los Filabres), indicating shortening, whereas velocities directed towards the west, decrease towards the south (e.g., between W-Sierra de los Filábres and Sierra de Gador), indicating extension and right-lateral shear. Triangles indicate the volcanic centers filled with the same color code as for the AHe ages. Contours of exposed upper Tortonian and Messinian-Pliocene limestones are also indicated. **b–e** QTQt-derived thermal histories were obtained (see Supplementary Data 3) for four samples representative of the thermal evolution of CGVP (MOJ1.1, MOJ1.2, and MOJ1.5) and NF complex (MOJ2.1). Black boxes represent thermal and age constraints. Observed and predicted uncorrected AHe ages are indicated below each model T-t path. See text for abbreviations.

water (i.e., fluids trapped in the sediment during its deposition and lithification), indicating fluid-rock interactions. This contrasts with the negative $\delta^{18}O_{water}$ (TA45, TA31) of about -5‰ VSMOW pointing to a contribution of meteoric water. Given the temporal overlap of U-Pb-dated fluids, we infer that the circulation of seawater and meteoric water alternated in time during the 3-Myr fluid-flow event. T_{47} estimates indicate these fluids precipitated at around $75 \pm 10\,°C$ (2σ of 5 °C) or $72\,°C \pm 15\,°C$ if the undated TA31 sample is included in the calculation. Assuming they are fluids emplaced before folding of host rocks, paleodepths of 1-1.5 km are inferred for fluids that precipitated during the Tortonian (TA24, TA38, TA41) and Pliocene (TA36, TA45) (Figs. 1d and 5). It has been argued that the northern flank of the Tabernas syncline hosting NF and AJ basement samples (TA38, TA41) was folded before the Serravallian-Lower Tortonian[43]. When associated with the lower Tortonian sample from the Tabernas ridge (TA24),

characterized by identical T_{47} and U-Pb age, we infer that these Tortonian fluids reflect a basin-scale thermal event consistent with regional gradients above 75 °C/km. We conclude that these pre-5 Ma fluids precipitated in association with regional palaeogeothermal gradients of >50 °C/km, locally rising above 75 °C/km on the flanks of the basins. Comparison with continental geotherms accounting for radiogenic crustal heat production, and transient cooling of the lithosphere, indicate that these shallow crustal gradients are consistent with steady-state temperature gradients of 55 °C/km computed for a 65-km-thick lithosphere, crustal thickness of 25 km, and a thermal-tectonic age of the lithosphere of 20 Ma (Supplementary Discussion). We predict a surface heat flow of 118 mW/m², which agrees with the measured current heat flow of 124 mW/m² in the EAB[69]. Note that this value requires a high mantle heat flux of 48 mW/m² which is 50% higher than the average European mantle heat flow[49]. The $\delta^{18}O_{water}$
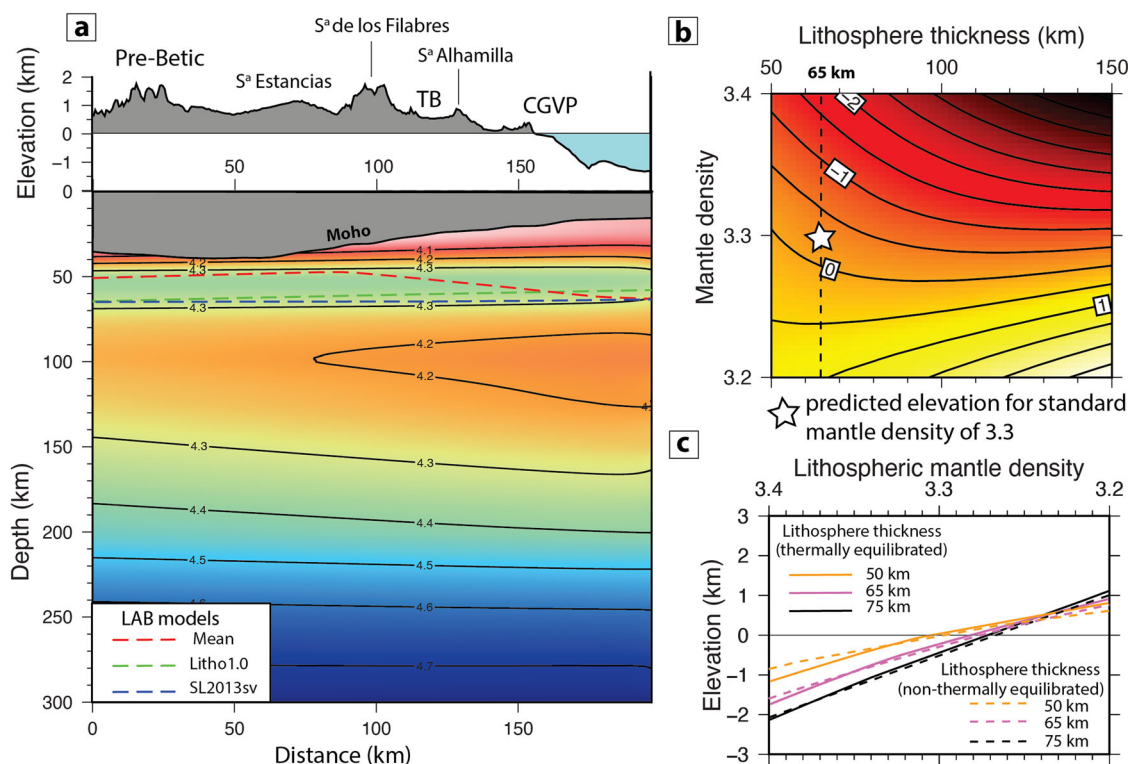
Fig. 5 | Lithospheric and sub-lithospheric architecture, and topography of the eastern Betics. a Topographic profile (see location in Fig. 1a), crustal thickness variations, and S-wave velocity structure from SL2013sv[44]. Values of S-wave velocities are indicated by contour lines and intervals of 0.1 km.s⁻¹. Dashed lines refer to the Lithosphere-Asthenosphere Boundary (LAB) inferred from different global seismologic models. Predicted elevation for variable lithosphere thickness and lithospheric mantle densities are shown as curves labeled in km **b** for crustal thickness of 25 km (crustal thickness below Tabernas Basin, TB). **c** Elevation as a function of mantle densities for variable lithosphere thickness, thermally and non-thermally equilibrated.

of the veins argue that fluids precipitated in equilibrium with the expected seawater and meteoric sources under a high regional continental geotherm established during lithosphere thinning and mantle upwelling.

These results combined with previous data show that basin subsidence and lithospheric thinning has continued from 8.5 and 5 Ma in the external basins of the Betics (Fig. 7), in contrast to the internal basins that recorded synchronous uplift and the closure of the marine gateway of the Betic Corridor. The distributed right-lateral strike-slip shearing (Fig. 1b) that is linked to lithospheric tearing and delamination, is likely to be the trigger of the contrasting vertical movements between internal and external basins (Fig. 7). Evidence for delamination is brought by geochemical and petrological data on the mantle sources of alkaline lavas. They show that the transition from calk-alkaline to high-K calc-alkaline, shoshonitic, and ultrapotassic volcanism occurred because of variable degrees of melting of a metasomatised lithospheric mantle prior to Paleogene collision in the Betics[70]. Delamination of the Iberian mantle, accompanied by upwelling of the asthenospheric mantle (Fig. 7), provides the most reliable explanation for the observed magmatic evolution. The Na-alkaline basalts are, however, linked to low-degree melting of the upwelling sub-lithospheric mantle[71]. Because of the differential motion between the retreating mantle delamination zone (Alboran) towards the west and the overriding plate (Iberia), propagating strike-slip faults resulted in lithospheric tearing in the sense of Govers and Wortel[72]. In the exposed crust, the tectonic interpretation of E-W dextral transfer fault zones, vertical rotations across the Internal and External Betics[73], and orogen-parallel extension supports this scenario. Recent research has established that tearing is distributed rather than localized, and that extension is oblique to the Betic trend, hence resulting in the formation of a highly oblique rifted margin[43].

Delamination and the origin and demise of the Messinian Salinity Crisis

We propose that the association of oblique extension in the distributed right-lateral strike-slip shear zone and delamination retreat, explains the contrast between the uplifted internal basins that developed on the thick proximal margin, and the subsidence of external basins that underwent larger rift-related extension (Fig. 7). The extension triggered by westward retreat of the slab that we constrain between 8 and 5 Ma in the eastern Betics is synchronous with the pre-MSC closure of marine corridors in Spain and in Morocco. In Morocco, uplift is attributed to transpression, which likely reflects the differential movement of the sinking slab relative to the motion of Africa[25]. Importantly, the mid-late Miocene stage of formation of the strike-slip transfer zone in the Betics is temporally distinct from the onset of slab tearing, which is a localized lithospheric feature that does not extend over the whole Betics, as imaged by seismic data (Fig. 1b). According to our interpretation, this tectonic configuration lasted until 5 Ma when the delaminated slab detached and shortening initiated in the Betics (Fig. 7). Extrusion of the Alboran block and onset of the CF developed at this time. It has been suggested that the transition from oceanic subduction to continental delamination was responsible for the change between the pre-MSC high-K calc-alkaline, shoshonitic, and ultrapotassic volcanism and the emplacement of the most primitive lavas, comprising the isolated emission of post-MSC Na-alkaline basalts (hawaiite) (2.9-2.3 Ma)[71]. In contrast, we argue that the 3 Myrs gap between pre-MSC and post-MSC magmatism observed in the eastern Betics (Fig. 6) is the consequence of shortening. The same timing of pre-MSC high-K calc-alkaline volcanism at ~6.6 Ma relative to post-MSC Si-poor volcanism at 4 Ma in Morocco[16,67,68] indicates that slab detachment and mantle
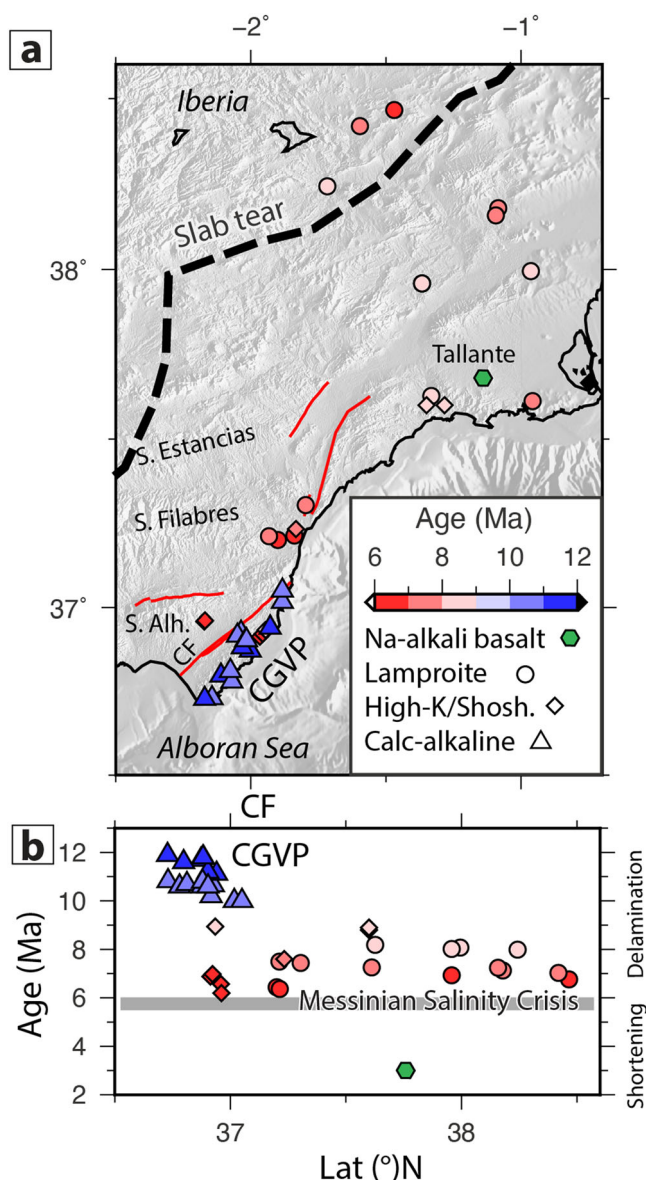
Fig. 6 | Geographic and temporal relationships between the different types of volcanism in eastern Betics. a Distribution of type and age of magmatism in the eastern Betics. **b** Same as (**a**) but with data projected relative to latitude. The timing of Messinian Salinity (MSC), delamination and crustal shortening are indicated.

upwelling, which are coincident with the shift to shortening, took place regionally.

The closure of the marine gateways in Spain and Morocco between 7.8 and 7.0 Ma occurred during the latest stages of continental delamination retreat initiated as early as 11 ± 1 Ma (onset of EAB magmatic arc) that was accompanied by extension in the Betics (Fig. 7) and shortening in the Rif. The remaining marine gateway supplying salt to the Mediterranean at the origin of the MSC is the Gibraltar gateway. We link the MSC to the progressive uplift of this marine corridor caused by a combination of lithospheric delamination and magmatism. This model agrees with the occurrence of an Alboran volcanic archipelago that permitted faunal exchanges before and after the MSC[28]. While the role of geodynamic processes in the Gibraltar region is central, the onset of the MSC further indicates the additional impact of global sea-level lowering and paleoclimate[74]. Following the rapid migration of the slab detachment in Spain and Morocco towards Gibraltar, slab pull forces increased in this region causing the subsidence and widening of the Gibraltar gateway. The slab detachment

event is therefore considered the cause of the demise of the MSC rather than its trigger. This post-5 Ma event was coincident with the formation of a new plate boundary fault between Africa and Iberia has so far produced limited regional effects on topography compared to deep mantle processes.

Methods
Samples
Calcite samples were collected in veins predominantly striking NW-SE and WNW-ESE opened perpendicular to the regional extension-oriented NE-SW determined from paleostress data[43] and in calcite steps on faults consistent with the same regional extension. Calcite veins are present in all the stratigraphic sections both in the basement and the overlying sedimentary series (Fig. 1d). Most veins are predominantly vertical (TA31, TA36, TA45, TA38) and locally at moderate angle (TA44) with respect to bedding, and their widths range from millimeters to centimeters (Figs. 2 and 3). The calcite crystals form generally elongated blocky syntaxial to fibrous textures (Supplementary Data 1). Fourteen slabs were prepared and polished thin sections were examined by conventional and cold cathodoluminescence microscopes to detect the different generations of crystallization/recrystallization and select the in-situ rock sample for further analyses. In most veins, one continuous single calcite phase precipitation (TA31, TA24, TA45, TA38, TA44) is observed indicating coeval opening and mineralization (Supplementary Data 1). Samples TA36 and TA41 have two generations of calcite (consistent with U-Pb analyses showing secondary late U-Pb ages, Supplementary Data 1).

Sampling for (U-Th)/He analyses has focused on the most felsic lavas in CGMP (andesite, dacite, rhyolite) (MOJ1.1, MOJ1.2, MOJ1.3, MOJ1.4, MOJ1.5) and in NF metamorphic complex (MOJ2.1) for comparing cooling histories across the Carboneras fault zone (see sample information and analyses in Supplementary Data 3). An attempt was made to select CGVP samples near marine carbonates of Tortonian-Messinian and lower Pliocene ages that were deposited after magma emplacement to place thermal constraints for modeling the post-Tortonian uplift and exhumation.

Calcite LA-ICP-MS U-Pb geochronology
Calcite U-Pb analyses were performed at the Geochronology & Tracers Facility, British Geological Survey (Nottingham, UK) using a Nu Instruments Attom single collector inductively coupled plasma mass spectrometer coupled to a NWR193UC laser ablation system fitted with a TV2 cell. Laser parameters were $100\,\mu m$ spots, ablated at 10 Hz for 30 s with a fluence of ~4 J cm^2 (see Supplementary Data 1 for full instrumental conditions). Normalization used WC1[75] as a primary reference material for Pb/U ratios and NIST614 for Pb/Pb ratios[76]; ASH15D[77] was run as a secondary reference material and the pooled result across the analytical sessions is within 2% accuracy of the accepted age. Data reduction uses the Time-Resolved-Analysis function in the Attolab software, followed by normalization offline in Excel. Age calculations and plotting use IsoplotR[78]. All ages are derived from lower intercept ages on Tera-Wasserburg plots (see Fig. 2 and Supplementary Data 1), quoted at 2σ and shown as $\pm\alpha/\beta$, where α and β are without and with systematic uncertainties, respectively. Several samples were analyzed but were not used in our study due to low U/Pb ratios hindering a robust age calculation, or to highly scattered analyses indicating age mixing and/or U mobility. All data are presented in Supplementary Data 1.

Clumped isotope analysis
All analyses were performed at the Laboratoire des Sciences du Climat et de l'Environnement (LSCE, Gif sur Yvette). Six samples (TA24, TA31, TA36, TA38, TA41, TA45) of homogenized carbonate powder were converted to CO_2 by phosphoric acid reaction at 90 °C in a common, stirred acid bath for 15 min. The initial phosphoric acid concentration was 103 % (1.91 g/cm^3) and each batch of acid was used for 7 days. After cryogenic
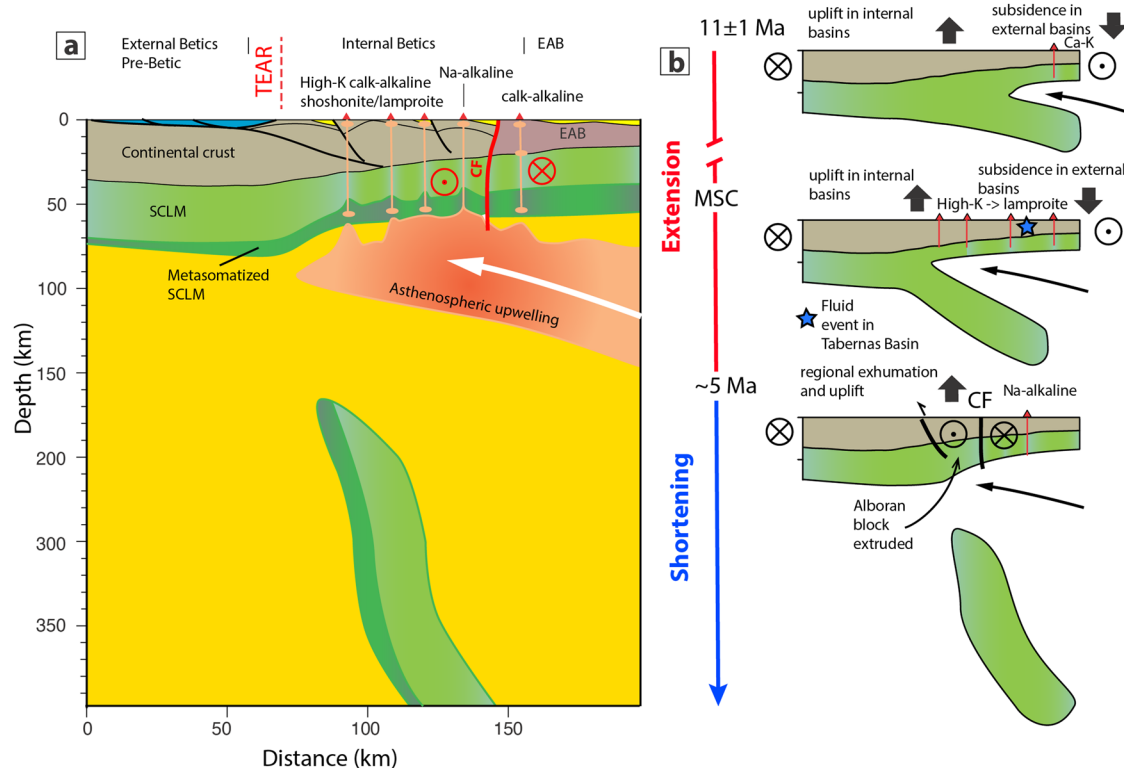
Fig. 7 | Deep lithospheric structure and tectono-magmatic evolution of the eastern Betics before, during, and after the MSC. a Present-day tectono-magmatic model of the eastern Betics along profile shown in Figs. 1 and 5. Note that the mantle slab is still attached below the western Betics (see Fig. 1b). **b** Tectonic scenario of the evolution of the eastern Betics from extension to onset of shortening and presenting key elements of the evolution of the mantle from retreating delamination to slab detachment before and surface processes before and after the MSC.

removal of water, the evolved CO_2 was helium-flushed at 25 mL/mn through a purification column packed with Porapak Q (50/80 mesh, 1 m length, 2.1 mm ID) and held at −20 °C, then quantitatively recollected by cryogenic trapping and transferred into an Isoprime 100 dual-inlet mass spectrometer equipped with six Faraday collectors (m/z 44–49). Each analysis took about 2.5 h, during which analyte gas and working reference gas were allowed to flow from matching, 10 mL reservoirs into the source through deactivated fused silica capillaries (65 cm length, 110 μm ID). Every 20 minutes, gas pressures were adjusted to achieve $m/z = 44$ current of 80 nA, with differences between analyte gas and working gas generally below 0.1 nA. Pressure-dependent background current corrections were measured 12 times for each analysis. All background measurements from a given session within ±6 hours of any given analysis were used to determine a mass-specific relationship for that analysis, linking background intensity (Zm), total $m/z = 44$ intensity (I44), and time (t): Zm = aI44 + P(t), with P being a polynomial of degree 2 to 4. Background-corrected ion current ratios (δ45 to δ49) were converted to $\delta^{13}C$, $\delta^{18}O$, and "raw" Δ_{47} values as described by Daëron et al.[79], using the IUPAC oxygen-17 correction parameters. The isotopic composition (δ13C, δ18O) of our working reference gas was computed based on the nominal isotopic composition of all ETH carbonate standards[80] and an oxygen-18 acid fractionation factor of 1.00813. Raw Δ_{47} values were then converted to the I-CDES reference frame[81] using a pooled regression approach as implemented by the Δ47crunch Python library. Full analytical errors are derived from the external reproducibility of unknowns and standards (Nf = 39) and conservatively account for the uncertainties in raw Δ_{47} measurements as well as those associated with the conversion to the I-CDES reference frame. T_{47} reconstructions are based on the OGLS23 calibration (see Supplementary Data 2). Temperature confidence intervals account for analytical error in Δ_{47} but not for calibration uncertainties, which remain below ±1 °C (95% CL) in the range 0–50 °C. The $\delta^{18}O$ values of

the mineralizing fluids ($\delta^{18}O_{water}$) are derived from T_{47} and the $\delta^{18}O_{CaCO3}$ of the mineral based on the fractionation equation.

Apatite (U-Th)/He dating

Separation and selection of apatites were carried out at the GET laboratory. Each sample was crushed to obtain grains smaller than 500 μm. Two successive steps of dense liquor separation followed to recover grains with a density between 2.97 and 3.38 (apatite density 3.2). This fraction was then magnetically sorted by Frantz. The remaining fraction, non-magnetic, was finally sorted by optical microscope (picking). Apatite crystals for (U-Th-Sm)/He dating were handpicked to select inclusion-free crystals with a minimum of three aliquots. Crystal dimension and geometry were measured along two axes, considering the apatite crystals as regular hexagonal prisms, grains had in general a minimum width of 60 μm to minimize the effect of alpha particle ejection. After this first step, (U-Th)/He analyses on apatite were performed at the Noble Gas Laboratory of the Geosciences Montpellier laboratory. Each grain, packed in Pt tubes, was placed under vacuum and heated for 5 minutes with a 1090 nm fiber laser operating at 4.0 W (900 °C). After spiking (addition of a known amount to be able to quantify the real content in the minerals) with 3He, gas purification was performed by a cryogenic trap and two AP-10-N SAES getters, and the helium content was measured on a PrismaPlus QMG 220 quadrupole. The 4He content was determined by the peak height method which is 10 to 10,000 times higher than typical blank levels. A second heating cycle using the same analytical procedure was routinely performed to verify that more than 99% of the 4He was extracted in the first cycle. After helium extraction, the Pt tubes were retrieved from the sample chamber and transferred to a 2 ml polypropylene conical tube. The samples were triple spiked (149Sm, 230Th, and 233U) and dissolved following the procedures described by Wu et al.[82]. The resulting solutions were diluted and U (233U and

238U), Th (230Th and 232Th), and Sm (149Sm and 147 Sm) were measured using ICPMS isotope dilution. For the age calculation, it is necessary to perform the alpha (4He) particle ejection correction. This correction was calculated using Ft software considering the size, and shape of each apatite[83,84]. Analyses are presented in Supplementary Data 3.

QTQt thermal modelling

Thermal histories were retrieved from AHe data analyses using thermal inversion QTQt modelling software[85]. For AHe, QTQt incorporates kinetic models for helium diffusion in apatite crystals that account for radiation damage production and annealing (see Supplementary Data 3 for reference). These two diffusion models may produce different results, depending on the integrated thermal history of each grain. The inversion procedure uses a Bayesian "Markov chain Monte Carlo" algorithm to determine the best time-temperature path reproducing our data through a large number (between 100,000 and 200,000 on average) of randomly tested solutions. In our case, we have run nearly 170,000 models. The final model is represented by a set of time-temperature histories for which we included the expected model (weighted mean model) and the maximum likelihood model (best data fitting model). A table summarizing the thermal history model input parameters and all thermal models is provided in Supplementary Data 3.

Isostatic calculation, Vs-temperature conversion, and dynamic topography

The topography of continents reflects the combined effects of (1) isostasy that results from the variation of age-dependent lithosphere thickness and densities and (2) a non-isostatic (dynamic) component caused by plate strength, subduction dynamics, or more broadly mantle flow driven by anomalously hot asthenosphere. The elevation, e, of a buoyant lithospheric column in Airy isostatic equilibrium, with respect to the average mid-ocean ridge depth, is given by

$$e = h_c\left(\frac{\rho_a - \rho_c}{\rho_a}\right) - h_{oc}\left(\frac{\rho_a - \rho_{oc}}{\rho_a}\right) - h_w\left(\frac{\rho_a - \rho_w}{\rho_a}\right) + (h_l - h_c)\left(\frac{\rho_a - \rho_m}{\rho_a}\right) \quad (1)$$

where ρ_c, ρ_{oc}, ρ_w, ρ_m, and h_c, h_{oc}, h_w, h_l are the densities and thickness of the crust, oceanic crust, water column above the mid-ocean ridge, and continental lithosphere, respectively. The calculation assumes the density of the asthenosphere ρ_a accounts for an adiabatic temperature gradient and for the effect of compressibility. ρ_m varies with depth according to a linear geotherm and accounts for the effect of depletion and compressibility. Elevation is calculated for the case of thermal equilibrium and the case of the instantaneous removal of the lithospheric material by delamination, assuming no thermal equilibration at the base of the original lithosphere[50]. An original lithosphere thickness of 100 km is consistent with the average thickness of Phanerozoic lithosphere. Equations and parameters are presented in Supplementary Discussion.

S-wave velocities from model SL2013sv are then used to calculate temperatures in the mantle using the parametrization of ref. [54]. V_s (P, Θ, a) is dependent on pressure P (depth, z), temperature Θ in °C and a which is a variable describing the activation process. V_s is given by

$$V_s = (1 - b_v(z - 50))\left(m\Theta + c + A\exp\left(\frac{-E - PV_a}{RT}\right)\right) \quad (2)$$

where empirical constants are $b_v = 3.84 \times 10^{-4}$ km^{-1}, $m = -0.28$ m.s^{-1} ∮C^{-1}, $c = 4720$ m.s^{-1}, $A = -1.8 \times 10^{16}$ m.s^{-1}, $E = 409 \times 10^3$ J.mol^{-1}, $V_a = 10 \times 10^{-6}$ m^3.mol^{-1} and R the gas constant is 8.3145 (see Supplementary Discussion). The highest temperature obtained is 1550 °C at 100–125 km below the Tabernas basin and to the south where V_s decrease to 4.2 km.s^{-1}.

Dynamic uplift U created by the temperature anomaly is then calculated assuming thermal expansivity from background temperature and Airy isostasy[86] using the following equation:

$$U = \frac{H\alpha\bar{T}}{1 - \alpha T_0} \quad (3)$$

where H is the layer thickness, α is the thermal expansivity, T_0 is the background temperature, and $\bar{T}$ is the average temperature in the low viscous asthenospheric channel produced by the excess in temperature (parameters are provided in Supplementary Discussion). For an average thermal anomaly of 100 and 200 km the predicted uplift ranges between 500 m and 1 km. Considering the elevation of −250 m predicted by isostasy assuming pressure-temperature dependent densities and chemical depletion for the lithospheric mantle, the range of dynamic uplift can produce the elevation of 500 m observed around Tabernas Basin.

Temperature of continental lithosphere and heat flux estimates

The continental geotherms T_{cont} is given by

$$T_{cont}(z, age, H_s) = T_{std}(z, H_s) + T(age) \quad (4)$$

It is calculated using the stationary part of the geotherm T_{std} and contribution due to the radiogenic heat production H_s in the crust, and correction $T(age)$ due to transient cooling of the lithosphere that depends on the age of the last major plate-scale thermal event.

Temperature T_m at Moho depth, h_c, is used for calculation of temperature at depths below the Moho and is given by:

$$T_m = T_0 + \frac{q_m}{k_c}h_c + T_r \quad (5)$$

where T_0 and q_m correspond to the temperature at the surface and the mantle heat flux calculated at the Moho depth. T_r is the radiogenic contribution that is dependent on the thickness of the crust h_c, density ρ_c, radiogenic production H_s, radiogenic production decay depth h_r, and thermal conductivity coefficient k_c according to the following equation:

$$T_r = \frac{\rho_c H_s h_r^2}{k_c}\left(1 - e^{\frac{h_c}{h_r}}\right) \quad (6)$$

Details on the calculation are given in Supplementary Discussion.

Data availability

The authors declare that source data are provided with this article and its supplementary information files.

References

1. Bird, P. Continental delamination and the Colorado Plateau. *J. Geophys. Res.: Solid Earth* **84**, 7561–7571 (1979).
2. Bird, P. Initiation of intracontinental subduction in the Himalaya. *J. Geophys. Res.: Solid Earth* **83**, 4975–4987 (1978).
3. Clift, P. D., Vannucchi, P. & Morgan, J. P. Crustal redistribution, crust–mantle recycling and Phanerozoic evolution of the continental crust. *Earth Sci. Rev.* **97**, 80–104 (2009).
4. Kay, R. W. & Kay, S. M. Delamination and delamination magmatism. *Tectonophysics* **219**, 177–189 (1993).
5. Jagoutz, O. & Behn, M. D. Foundering of lower island-arc crust as an explanation for the origin of the continental Moho. *Nature* **504**, 131–134 (2013).
6. Jagoutz, O. & Kelemen, P. B. Role of Arc processes in the formation of continental crust. *Annu. Rev. Earth Planet. Sci.* **43**, 363–404 (2015).

7. Chowdhury, P., Gerya, T. & Chakraborty, S. Emergence of silicic continents as the lower crust peels off on a hot plate-tectonic Earth. *Nat. Geosci.* **10**, 698–703 (2017).

8. Chelle-Michou, C., McCarthy, A., Moyen, J.-F., Cawood, P. A. & Capitanio, F. A. Make subductions diverse again. *Earth-sci. Rev.* **226**, 103966 (2022).

9. Le Pourhiet, L., Gurnis, M. & Saleeby, J. Mantle instability beneath the Sierra Nevada Mountains in California and Death Valley extension. *Earth Planet. Sci. Lett.* **251**, 104–119 (2006).

10. Zandt, G. et al. Active foundering of a continental arc root beneath the southern Sierra Nevada in California. *Nature* **431**, 41–46 (2004).

11. Platt, J. P. & England, P. C. Convective removal of lithosphere beneath mountain belts; thermal and mechanical consequences. *Am. J. Sci.* **294**, 307–336 (1994).

12. Chiarabba, C. & Chiodini, G. Continental delamination and mantle dynamics drive topography, extension and fluid discharge in the Apennines. *Geology* **41**, 715–718 (2013).

13. Serri, G., Innocenti, F. & Manetti, P. Geochemical and petrological evidence of the subduction of delaminated Adriatic continental lithosphere in the genesis of the Neogene-Quaternary magmatism of central Italy. *Tectonophysics* **223**, 117–147 (1993).

14. Calvert, A. et al. Geodynamic evolution of the lithosphere and upper mantle beneath the Alboran region of the western Mediterranean: constraints from travel time tomography. *J. Geophys. Res.: Solid Earth* **105**, 10871–10898 (2000).

15. Duggen, S., Hoernle, K., Bogaard, P., van den, Rüpke, L. & Morgan, J. P. Deep roots of the Messinian salinity crisis. *Nature* **422**, 602–606 (2003).

16. Duggen, S., Hoernle, K., Bogaard, Pvanden & Harris, C. Magmatic evolution of the Alboran region: the role of subduction in forming the western Mediterranean and causing the Messinian Salinity Crisis. *Earth Planet Sc. Lett.* **218**, 91–108 (2004).

17. Valera, J.-L., Negredo, A.-M., & Villaseñor, A. Asymmetric delamination and convective removal numerical modeling: comparison with evolutionary models for the Alboran Sea region. *Pure Appl. Geophys.* **165**, 1683–1706 (2008).

18. Whitney, D. L. et al. Breaking plates: creation of the East Anatolian fault, the Anatolian plate, and a tectonic escape system. *Geology* **51**, 673–677 (2023).

19. Keskin, M. Magma generation by slab steepening and breakoff beneath a subduction-accretion complex: an alternative model for collision-related volcanism in Eastern Anatolia, Turkey. *Geophys. Res. Lett.* **30**, 8046 (2003).

20. Göğüş, O. H. & Pysklywec, R. N. Mantle lithosphere delamination driving plateau uplift and synconvergent extension in eastern Anatolia. *Geology* **36**, 723–726 (2008).

21. Faccenna, C., Bellier, O., Martinod, J., Piromallo, C. & Regard, V. Slab detachment beneath eastern Anatolia: a possible cause for the formation of the North Anatolian fault. *Earth Planet Sc. Lett.* **242**, 85–97 (2006).

22. Garcia-Castellanos, D. & Villaseñor, A. Messinian salinity crisis regulated by competing tectonics and erosion at the Gibraltar arc. *Nature* **480**, 359–363 (2012).

23. Krijgsman, W. et al. The Gibraltar corridor: watergate of the Messinian salinity crisis. *Mar. Geol.* **403**, 238–246 (2018).

24. Capella, W. et al. Palaeogeographic evolution of the late Miocene Rifian Corridor (Morocco): reconstructions from surface and subsurface data. *Earth Sci. Rev.* **180**, 37–59 (2018).

25. Spakman, W., Chertova, M. V., van den Berg, A. & van Hinsbergen, D. J. Puzzling features of western Mediterranean tectonics explained by slab dragging. *Nat. Geosci.* **11**, 211–216 (2018).

26. GómezdelaPeña, L. et al. Evidence for a developing plate boundary in the western Mediterranean. *Nat. Commun.* **13**, 4786 (2022).

27. Boonma, K., García-Castellanos, D., Jiménez-Munt, I. & Gerya, T. Thermomechanical modelling of lithospheric slab tearing and its topographic response. *Front. Earth Sci.* **11**, 1095229 (2023).

28. Booth-Rea, G., Ranero, C. R. & Grevemeyer, I. The Alboran volcanic-arc modulated the Messinian faunal exchange and salinity crisis. *Sci. Rep.* **8**, 13015 (2018).

29. Borque, M. J. et al. How much Nubia-Eurasia convergence is accommodated by the NE End of the Eastern Betic Shear Zone (SE Spain)? constraints from GPS velocities. *Tectonics* **38**, 271–1839 (2019).

30. Palano, M., González, P. J. & Fernández, J. The diffuse plate boundary of Nubia and Iberia in the Western Mediterranean: crustal deformation evidence for viscous coupling and fragmented lithosphere. *Earth Planet. Sci. Lett.* **430**, 439–447 (2015).

31. Platt, J. P., Whitehouse, M. J., Kelley, S. P., Carter, A. & Hollick, L. Simultaneous extensional exhumation across the Alboran Basin: implications for the causes of late orogenic extension. *Geology* **31**, 251–254 (2003).

32. Larrey, M. et al. Oblique rifting triggered by slab tearing: the case of the Alboran rifted margin in the eastern Betics. *Solid Earth* **14**, 1221–1244 (2023).

33. Mancilla, F. et al. Slab rupture and delamination under the Betics and Rif constrained from receiver functions. *Tectonophysics* **663**, 225–237 (2015).

34. Weijermars, R., Roep, T. B., Van den Eeckhout, B., Postma, G. & Kleverlaan, K. Uplift history of a Betic fold nappe inferred from Neogene-Quaternary sedimentation and tectonics (in the Sierra Alhamilla and Almeria, Sorbas and Tabernas Basins of the Betic Cordilleras, SE Spain). *Geol. Mijnb.* **64**, 397–411 (1985).

35. Platt, J. P., Kelley, S. P., Carter, A. & Orozco, M. Timing of tectonic events in the Alpujárride Complex, Betic Cordillera, southern Spain. *J. Geol. Soc. Lond.* **162**, 451–462 (2005).

36. Vázquez, M., Jabaloy, A., Barbero, L. & Stuart, F. M. Deciphering tectonic- and erosion-driven exhumation of the Nevado-Filábride complex (Betic Cordillera, Southern Spain) by low temperature thermochronology: deciphering tectonic- and erosion-driven exhumation. *Terra Nova* **23**, 257–263 (2011).

37. Shuster, D. L., Flowers, R. M. & Farley, K. A. The influence of natural radiation damage on helium diffusion kinetics in apatite. *Earth Planet. Sci. Lett.* **249**, 148–161 (2006).

38. Zeck, H. P., Maluski, H. & Kristensen, A. B. Revised geochronology of the Neogene calc-alkaline volcanic suite in Sierra de Gata, Alborán volcanic province, SE Spain. *J. Geol. Soc. Lond.* **157**, 75–81 (2000).

39. Martín, J. M., Braga, J. C. & Betzler, C. Late Neogene–Recent uplift of the Cabo de Gata volcanic province, Almería, SE Spain. *Geomorphology* **50**, 27–42 (2003).

40. Braga, J. C., Martín, J. M. & Quesada, C. Patterns and average rates of late Neogene–Recent uplift of the Betic Cordillera, SE Spain. *Geomorphology* **50**, 3–26 (2003).

41. Arribas, A. et al. Geology, geochronology, fluid inclusions, and isotope geochemistry of the Rodalquilar gold alunite deposit, Spain. *Econ. Geol.* **90**, 795–822 (1995).

42. Diaz, J., Gallart, J. & Carbonell, R. Moho topography beneath the Iberian-Western Mediterranean region mapped from controlled-source and natural seismicity surveys. *Tectonophysics* **692**, 74–85 (2016).

43. Larrey, M. et al. Oblique rifting triggered by slab tearing and back-arc extension: the case of the Alboran rift in the eastern Betics. *Egusphere* **2022**, 1–39 (2022).

44. Schaeffer, A. J. & Lebedev, S. Global shear speed structure of the upper mantle and transition zone. *Geophys. J. Int.* **194**, ggt095–ggt449 (2013).

45. Pasyanos, M. E., Masters, T. G., Laske, G. & Ma, Z. LITHO1.0: an updated crust and lithospheric model of the Earth. *J. Geophys. Res.: Solid Earth* **119**, 2153–2173 (2014).

46. Steinberger, B. & Becker, T. W. A comparison of lithospheric thickness models. *Tectonophysics* **746**, 325–338 (2016).

47. Thurner, S., Palomeras, I., Levander, A., Carbonell, R. & Lee, C. Ongoing lithospheric removal in the western Mediterranean: evidence from Ps receiver functions and thermobarometry of Neogene basalts (PICASSO project). *Geochem. Geophys. Geosyst.* **15**, 1113–1127 (2014).

48. O'Reilly, S. Y. & Griffin, W. L. Imaging global chemical and thermal heterogeneity in the subcontinental lithospheric mantle with garnets and xenoliths: geophysical implications. *Tectonophysics* **416**, 289–309 (2006).

49. Mouthereau, F. et al. Cenozoic mountain building and topographic evolution in Western Europe: impact of billions of years of lithosphere evolution and plate kinematics. *BSGF - Earth Sci. Bull.* **192**, 56 (2021).

50. McNab, F., Ball, P. W., Hoggard, M. J. & White, N. J. Neogene uplift and magmatism of anatolia: insights from drainage analysis and basaltic geochemistry. *Geochem. Geophys. Geosyst.* **19**, 175–213 (2018).

51. Molinari, I. & Morelli, A. EPcrust: a reference crustal model for the European Plate. *Geophys. J. Int.* **185**, 352–364 (2011).

52. Chenin, P. et al. Potential role of lithospheric mantle composition in the Wilson cycle: a North Atlantic perspective. *Geol. Soc. Lond. Spec. Publ.* **470**, 157–172 (2018).

53. Bianchini, G., Beccaluva, L., Nowell, G. M., Pearson, D. G. & Siena, F. Mantle xenoliths from Tallante (Betic Cordillera): insights into the multi-stage evolution of the south Iberian lithosphere. *Lithos* **124**, 308–318 (2011).

54. Priestley, K. & McKenzie, D. The thermal structure of the lithosphere from shear wave velocities. *Earth Planet. Sci. Lett.* **244**, 285–301 (2006).

55. Iribarren, L., Vergés, J. & Fernàndez, M. Sediment supply from the Betic–Rif orogen to basins through Neogene. *Tectonophysics* **475**, 68–84 (2009).

56. Garcés, M., Krijgsman, W. & Agustí, J. Chronology of the late Turolian deposits of the Fortuna basin (SE Spain): implications for the Messinian evolution of the eastern Betics. *Earth Planet Sc. Lett.* **163**, 69–81 (1998).

57. Flecker, R. et al. Evolution of the Late Miocene Mediterranean–Atlantic gateways and their impact on regional and global environmental change. *Earth-sci. Rev.* **150**, 365–392 (2015).

58. Clauzon, G. et al. New insights on the Sorbas Basin (SE Spain): the onshore reference of the Messinian Salinity Crisis. *Mar. Pet. Geol.* **66**, 71–100 (2015).

59. Do Couto, D. et al. Tectonic inversion of an asymmetric graben: insights from a combined field and gravity survey in the Sorbas basin. *Tectonics* **33**, 1360–1385 (2014).

60. Giaconia, F. et al. Compressional tectonic inversion of the Algero-Balearic basin: latemost Miocene to present oblique convergence at the Palomares margin (Western Mediterranean): tectonic inversion of palomares margin. *Tectonics* **34**, 1516–1543 (2015).

61. Martínez-García, P., Comas, M., Lonergan, L. & Watts, A. B. From extension to shortening: tectonic inversion distributed in time and space in the Alboran Sea, Western Mediterranean. *Tectonics* **36**, 2777–2805 (2017).

62. Clark, S. J. P. & Dempster, T. J. The record of tectonic denudation and erosion in an emerging orogen: an apatite fission-track study of the Sierra Nevada, southern Spain. *J. Geol. Soc.* **166**, 87–100 (2009).

63. Reinhardt, L. J., Dempster, T. J., Shroder, J. F. & Persano, C. Tectonic denudation and topographic development in the Spanish Sierra Nevada. *Tectonics* **26**, n/a-n/a (2007).

64. Janowski, M. et al. Neogene exhumation and relief evolution in the eastern Betics (SE Spain): insights from the Sierra de Gador. *Terra Nova* **29**, 91–97 (2017).

65. Johnson, C., Harbury, N. & Hurford, A. J. The role of extension in the Miocene denudation of the Nevado-Filábride Complex, Betic Cordillera (SE Spain). *Tectonics* **16**, 189–204 (1997).

66. Sendra, J., Reolid, M. & Reolid, J. Palaeoenvironmental interpretation of the Pliocene fan-delta system of the Vera Basin (SE Spain): fossil assemblages, ichnology and taphonomy. *Palaeoworld* **29**, 769–788 (2020).

67. Turner, S. P. et al. Magmatism associated with orogenic collapse of the Betic-Alboran domain, SE Spain. *J. Petrol.* **40**, 1011–1036 (1999).

68. Duggen, S. et al. Geochemical zonation of the Miocene Alborán Basin volcanism (westernmost Mediterranean): geodynamic implications. *Contrib. Miner. Petr.* **156**, 577 (2008).

69. Polyak, B. G. et al. Heat flow in the Alboran Sea, western Mediterranean. *Tectonophysics* **263**, 191–218 (1996).

70. Conticelli, S. et al. Trace elements and Sr–Nd–Pb isotopes of K-rich, shoshonitic, and calc-alkaline magmatism of the Western Mediterranean Region: genesis of ultrapotassic to calc-alkaline magmatic associations in a post-collisional geodynamic setting. *Lithos* **107**, 68–92 (2009).

71. Duggen, S., Hoernle, K., vandenBogaard, P. & Garbe-Schönberg, D. Post-collisional transition from subduction- to intraplate-type magmatism in the Westernmost Mediterranean: evidence for continental-edge delamination of subcontinental lithosphere. *J. Petrol.* **46**, 1155–1201 (2005).

72. Govers, R. & Wortel, M. J. R. Lithosphere tearing at STEP faults: response to edges of subduction zones. *Earth Planet Sc. Lett.* **236**, 505–523 (2005).

73. Crespo-Blanc, A., Comas, M. & Balanyá, J. C. Clues for a Tortonian reconstruction of the Gibraltar Arc: structural pattern, deformation diachronism and block rotations. *Tectonophysics* **683**, 308–324 (2016).

74. Krijgsman, W. et al. Causes and consequences of the Messinian salinity crisis. *Nat. Rev. Earth Environ.* **5**, 335–350 (2024).

75. Roberts, N. M. W. et al. A calcite reference material for LA-ICP-MS U-Pb geochronology. *Geochem. Geophys. Geosyst.* **18**, 2807–2814 (2017).

76. Woodhead, J. D. & Hergt, J. M. Strontium, neodymium and lead isotope analyses of NIST glass certified reference materials: SRM 610, 612, 614. *Geostand. Newsl.* **25**, 261–266 (2001).

77. Nuriel, P. et al. The use of ASH-15 flowstone as a matrix-matched reference material for laser-ablation U-Pb geochronology of calcite. *Geochronology* **3**, 35–47 (2021).

78. Vermeesch, P. IsoplotR: a free and open toolbox for geochronology. *Geosci. Front.* **9**, 1479–1493 (2018).

79. Daëron, M., Blamart, D., Peral, M. & Affek, H. P. Absolute isotopic abundance ratios and the accuracy of $\Delta 47$ measurements. *Chem. Geol.* **442**, 83–96 (2016).

80. Bernasconi, S. M. et al. Reducing uncertainties in carbonate clumped isotope analysis through consistent carbonate-based standardization. *Geochem. Geophys. Geosyst.* **19**, 2895–2914 (2018).

81. Bernasconi, S. M. et al. InterCarb: a community effort to improve interlaboratory standardization of the carbonate clumped isotope thermometer using carbonate standards. *Geochem. Geophys. Geosyst. G(3)* **22**, e2020GC009588 (2021).

82. Wu, L. et al. Cenozoic exhumation history of Sulu terrane: implications from (U–Th)/He thermochrology. *Tectonophysics* **672**, 1–15 (2016).

83. Gautheron, C. & Tassan-Got, L. A Monte Carlo approach to diffusion applied to noble gas/helium thermochronology. *Chem. Geol.* **273**, 212–224 (2010).

84. Ketcham, R. A., Gautheron, C. & Tassan-Got, L. Accounting for long alpha-particle stopping distances in (U–Th–Sm)/He geochronology: refinement of the baseline case. *Geochim. Cosmochim. Acta* **75**, 7779–7791 (2011).

85. Gallagher, K. Transdimensional inverse thermal history modeling for quantitative thermochronology. *J. Geophys. Res. Solid Earth*, https://doi.org/10.1029/2011JB008825 (2012).

86. Rudge, J. F., Champion, M. E. S., White, N., McKenzie, D. & Lovell, B. A plume model of transient diachronous uplift at the Earth's surface. *Earth Planet. Sci. Lett.* **267**, 146–160 (2008).

87. Alonso-Zarza, A. M. & Calvo, J. P. Palustrine sedimentation in an episodically subsiding basin: the Miocene of the northern Teruel Graben (Spain). *Palaeogeogr. Palaeoclim. Palaeoecol.* **160**, 1–21 (2000).

88. Ghetti, P. et al. The Early Messinian Velona basin (Siena, central Italy): paleoenvironmental and paleobiogeographical reconstructions. *Palaeogeogr. Palaeoclim. Palaeoecol.* **187**, 1–33 (2002).

89. Sánchez-Almazo, I. M., Spiro, B., Braga, J. C. & Martín, J. M. Constraints of stable isotope signatures on the depositional palaeoenvironments of upper Miocene reef and temperate carbonates in the Sorbas Basin, SE Spain. *Palaeogeogr. Palaeoclim. Palaeoecol.* **175**, 153–172 (2001).

90. Evans, N. P. et al. Coupled measurements of δ 18O and δD of hydration water and salinity of fluid inclusions in gypsum from the Messinian Yesares Member, Sorbas Basin (SE Spain). *Earth Planet. Sci. Lett.* **430**, 499–510 (2015).

Acknowledgments

Author contributions

F.M., L.B. and M.L. have conceived the project and developed the conceptual model. F.M., M.L. and L.B. collected the samples. M.L., L.B., S.B., N.E.B., D.H., N.M.W.R. and M.D. analyzed the samples. N.E.B. and D.H. interpreted the isotope data. N.M.W.R. and M.D. critically reviewed and interpreted the U-Pb and Δ_{47} analyses, respectively. F.M. developed the model with L.B. and F.M. wrote the manuscript with contributions from all the authors.

Competing interests

The authors declare no competing interests.

Additional information

Supplementary information The online version contains supplementary material available at https://doi.org/10.1038/s41467-025-59481-z.

Correspondence and requests for materials should be addressed to Frédéric Mouthereau.

Peer review information *Nature Communications* thanks Wout Krijgsman, and the other, anonymous, reviewer(s) for their contribution to the peer review of this work. A peer review file is available.

Reprints and permissions information is available at http://www.nature.com/reprints

Publisher's note Springer Nature remains neutral with regard to jurisdictional claims in published maps and institutional affiliations.